IEEE Access
Multidisciplinary ⋮ Rapid Review ⋮ Open Access Journal

Received October 18, 2021, accepted November 9, 2021, date of publication November 12, 2021, date of current version November 22, 2021.

*Digital Object Identifier 10.1109/ACCESS.2021.3127898*

# 3D Characteristic Analysis of 3-Leg Linear Permanent Magnet Motor With Magnet Skew and Overhang Structure

**KI-HOON KIM[1], (Student Member, IEEE), HYUN-KYU CHO[2], AND DONG-KYUN WOO[1]**
[1]Department of Electrical Engineering, Yeungnam University, Gyeongsan-si, Gyeongbuk 38541, South Korea
[2]Prestoliteasia, Icheon-si, Gyeonggi-do 17405, South Korea

Corresponding author: Dong-Kyun Woo (wdkyun@yu.ac.kr)

This work was supported in part by the 2021 Yeungnam University Research Grant.

**ABSTRACT** This paper presents the 3-leg linear permanent magnet motor (TLPMM), which has a novel structure. It has an advantage of reducing the entire volume due to the attraction force cancellation. The TLPMM consists of stator and mover modules, simplifying the manufacturing process and maintenance. The TLPMM has a permanent magnet skew and overhang structure to improve motor performance. Therefore, the consideration of three dimension (3D) effects is required in the characteristic analysis. The proposed method is based on a field reconstruction method that provides a reduction in computational burden with high accuracy in analyzing 3D characteristics. For the evaluation of magnetic fields in non-uniform and complex air-gap in the TLPMM, the virtual air-gap section method is introduced. Using these proposed methods, the TLPMM with the magnet skew and overhang structure are effectively analyzed. This approach was verified by comparison with finite element analysis and experimental results.

**INDEX TERMS** 3-leg linear permanent magnet motor, magnet skew, overhang effect, virtual air-gap section method.

## I. INTRODUCTION

A linear permanent magnet motor (LPMM) has been widely used in various applications where linear motion is required [1]. Given that the target performance of a linear motor varies depending on the usage environment, high thrust density along with low attractive force can be an important factor for technical requirements [2], [3]. In Fig. 1, the 3-leg linear permanent magnet motor (TLPMM) has a structure for the attractive force cancellation. This can reduce the support structure needed to keep the mover in place and allow it to move along its axis. It consists of two arrays of permanent magnets (PM) perpendicular to the direction of movement. The structure of the stator and the mover can be minimized to a module, simplifying the manufacturing process and maintenance. By adding modules in the horizontal or vertical direction, the performance can be improved, allowing flexible responses to various requirements.

In the TLPMM, PM overhang and skew are applied to improve thrust and reduce detent force. The structural complexity and the fact that overhang and PM skew require a 3D field analysis to accurately interpret the characteristics of the TLPMM. For this reason, a suitable analysis method is needed to determine the effective overhang length and skew angle while reducing computational time.

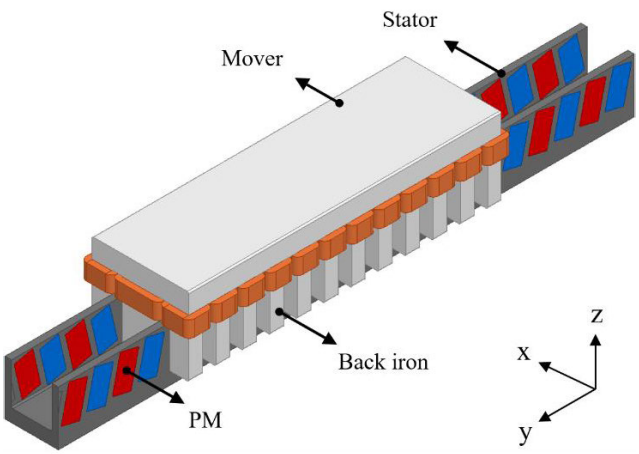


**FIGURE 1.** TLPMM topology.

The associate editor coordinating the review of this manuscript and approving it for publication was Wei Xu.


This work is licensed under a Creative Commons Attribution 4.0 License. For more information, see https://creativecommons.org/licenses/by/4.0/

An accurate calculation of air-gap magnetic flux density is one of the essential tasks as it is a prerequisite for predicting the thrust and attractive force. The previous researches related to the LPMM focused predominantly on analyzes of those with conventional shapes, such as flat and tubular linear motors [4], [5]. However, since the non-uniformity of the magnetic flux distribution in the TLPMM is caused not only by the ends in the moving direction, but also by all the ends of the complex air-gap, a more rigorous analysis of the detent force is demanded. For precise calculations of the air-gap magnetic flux density, the TLPMM requires computationally expensive 3D finite element (FE) analysis, which is not suitable for reasonable optimization design. To address this problem, this paper adopts the field reconstruction method (FRM).

The FRM is a FE-based analytical method for effective calculation of air-gap magnetic flux density, and can reduce the computational burden of FE calculation [6]. In the FRM, the total air-gap flux density consists of a field of independent elements such as individual PM and each slot winding. Each field is reconstructed by a basis function, which sweeps a snapshot of the reference magnetic flux distribution using static FE analysis. In addition, by using the basis function, it is possible to calculate the air-gap magnetic flux distribution at any excitation current or mover position without the additional FE analysis [7]–[9].

The proposed FE-based analytical model using the FRM enables the process of predicting the performance of the combination of modules by evaluating the magnetic flux distribution corresponding to each module in a short time. In Section III, the virtual air-gap section method is used to deal with the non-uniform air-gap magnetic flux density of the TLPMM. Since the virtual air-gap section method effectively evaluates the magnetic flux distribution in non-uniform air-gaps, it is applicable not only to the TLPMM but also to any models with complex structures.

Most LPMMs, including the TLPMM, have a different length of the stator and mover, which causes magnetic flux distortion at the end of the moving direction called end effect. In the case of the TLPMM, this end effect occurs at the end face of the back-iron of the mover, and the resulting end force contributes to the overall detent force. The optimal skew angle is determined depending on the waveform of the detent force. Therefore, in order to determine the optimal skew length of the PM, the contribution of this end force to the total detent force should be analyzed. In addition, since the optimal length of the PM skew depends on the overhang length in the TLPMM, this paper provides a comparative analysis of the PM skew and overhang length.

In Section II, the structure and characteristic of the TLPMM are introduced. In Section III, we propose a method to evaluate the air-gap magnetic flux distribution using the virtual air-gap section, and in Section IV, we introduce a method to calculate the force of the TLPMM. The effective overhang length and skew angle in Section V are provided with comparative analysis, and the validity of the analytical model was verified by comparison with the experimental results of the prototype produced in Section VI.

## II. PROTOTYPE MACHINES

To reduce the detent force of the LPMM, previous approaches have focused on adding auxiliary pole, semi-closed slot structure, changed length of the back-iron and PM skew [10]–[14]. Inoue *et al*. [10] presented the adjustment of the magnetic length to offset both end force of the stator back-iron. Although this method reduces the total detent force due to the cancellation of the end force, it results in an imbalance in the thrust due to the distortion of the armature field. Kim *et al*. [11] proposed the semi-closed slot method to reduce the detent force.

However, due to the structural characteristics of the TLPMM, it is impossible to manufacture the shoe and it does not have a significant effect compared to other methods. Boduroglu *et al*. [12], [13] used auxiliary poles at both ends of the stator back-iron, and presented step skew method. Among these, the PM skew method provides the greatest performance improvement with ease of workability [14]. In particular, the PM skew in a linear machine can be obtained simply by rotating a rectangular PM rather than a rhombus shape.

In the TLPMM, PM skew and overhang structure were applied to improve the motor performance. The overhang structure is used to increase the thrust by compensating for the decrease in magnetic flux density due to magnetic flux leakage at the axial end of the back-iron [15]–[18]. Unlike the conventional LPMM and rotating machine, the overhang in the TLPMM is applied only to one end of the PM, thereby making asymmetric magnetic flux density on the effective air-gap.

In the stator of the TLPMM, two rows of PM are arranged and are perpendicular to the floor surface. In order to reduce detent force and increase thrust, PMs rotate corresponding to the skew angle and have an overhang structure in the downward direction.

For symmetrical electromagnetic characteristic, two parallel PM arrays are skewed in opposite directions. The back-iron core has three legs and provides easy winding. Each core composed of a stacked back-iron is isolated from each other by a non-magnetic material.

Since the TLPMM has zero attraction force between the mover and the stator, it has the advantage of reducing the volume of the support structure that fixes the mover. Considering that the mover and stator are composed of a module, it is easy to assemble, manufacture and maintain. By adding modules in the axial or transverse direction, various performances can also be achieved.

The TLPMM has a structure that cannot be analyzed in 2D, such as the multi-air-gap and the overhang structure. Given that 3D FE analysis requires relatively expensive computation time, an effective approach is required for the analysis and design of these complex structures.

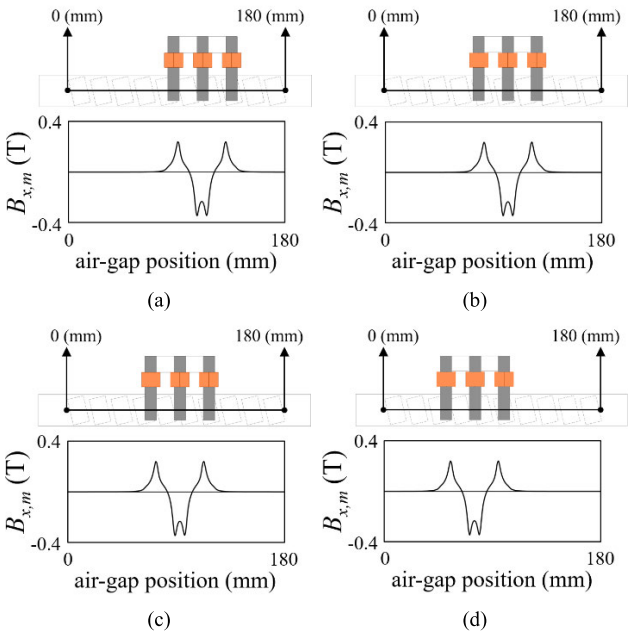


**FIGURE 2.** Armature reaction field of TLPMM. (a) The mover is in initial position. (b) Moved by 1/2 $\tau_p$. (c) Moved by $\tau_p$. (d) Moved by 2 $\tau_s$.

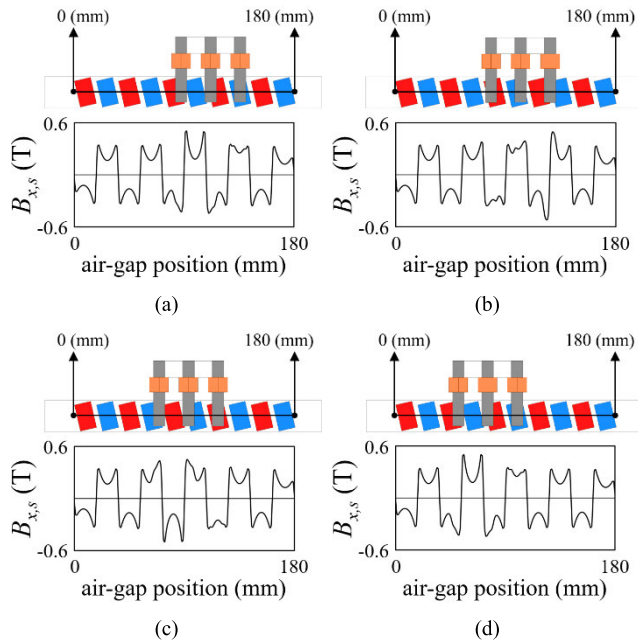


**FIGURE 3.** Open-circuit field of TLPMM. (a) The mover is in initial position. (b) Moved by 1/2 $\tau_p$. (c) Moved by $\tau_p$. (d) Moved by 2 $\tau_s$.

## III. ANALYSIS OF MAGNETIC FLUX DISTRIBUTION

In the TLPMM, an air-gap magnetic flux density is expressed as follows [19], [20]:

$$B_x(t,x,y,z) = B_{x,m}(t,x,y,z) + B_{x,s}(t,x,y,z) \quad (1)$$

$$B_y(t,x,y,z) = B_{y,m}(t,x,y,z) + B_{y,s}(t,x,y,z) \quad (2)$$

$$B_z(t,x,y,z) = B_{z,m}(t,x,y,z) + B_{z,s}(t,x,y,z) \quad (3)$$

where $B_x$, $B_y$, and $B_z$ are the $x$-, $y$-, and $z$-components of the total air-gap magnetic flux density, respectively, $B_m$ and $B_s$ are the air-gap magnetic flux density generated by armature reaction and PM, respectively. The total air-gap magnetic flux density is expressed as the sum of the independent magnetic flux densities of $B_m$ and $B_s$. $B_m$ and $B_s$ are the air-gap magnetic flux densities reconstructed by their respective basis functions. The basis function reconstructs the air-gap magnetic flux distribution corresponding to an arbitrary mover position or excitation current by storing the minimum information of the magnetic field.

### A. ARMATURE REACTION FIELD

The basis function sweeps the reference magnetic flux distribution to reconstruct the magnetic field. The reference magnetic flux distribution includes the structure information of slots and PM arrays. In the armature reaction field, it can be obtained through the FE analysis of the air-gap magnetic field generated from the DC excitation current of the individual winding excluding PM. On the other hand, in the open-circuit field, it can be obtained in the no-load condition with no excitation current. In the armature reaction field, the field reconstruction using the basis function is performed as follows:

$$B_m(t,x,y,z) = \sum_{a=1}^{N_s} f_{m,a}\left(x,y,z,B_{m,ref.}(x,y,z)\right) \cdot i_a(t) \quad (4)$$

where $f_{m,a}$ is the basis function of the armature reaction field generated by the $a$th winding current, $i_a$ is the excitation current in the $a$th slot, $N_s$ is the number of slots, and $B_{m.ref.}$ is the reference magnetic flux distribution of the mover.

The armature reaction field is the sum of the magnetic fields resulting from the excitation current of each slot winding of the mover. $f_{m,a}$ sweeps $B_{m.ref.}$ to reconstruct the entire armature reaction field. $B_{m.ref.}$ is obtained by a static FE analysis without PMs as follows:

$$B_{m,ref.} = \frac{B_m(t_0, I_0)}{I_0} \quad (5)$$

where $I_0$ and $t_0$ are the initial current and initial time, respectively. It is noted that $B_{m.ref.}$ is a static field containing structural information at the initial position.

Fig. 2 shows the armature reaction field in the air-gap at different mover positions. The movers are located in the initial position, 1/2 $\tau_p$, $\tau_p$, and 2 $\tau_p$, respectively, and $\tau_p$ is the pole pitch. The initial DC current $I_0 = 10$ A is excited, and PM is excluded.

Since the stator of the TLPMM is composed of PM and non-magnetic material, the air-gap flux distribution excluding PM is not affected by the position of the mover. The air-gap magnetic flux distribution at arbitrary mover position is shifted as follows:

$$B_{m,ref.}(t,x,y,z) = B_{m,ref.}(t_0, x, y + v \cdot t, z) \quad (6)$$

where $v$ is the velocity of the TLPMM.

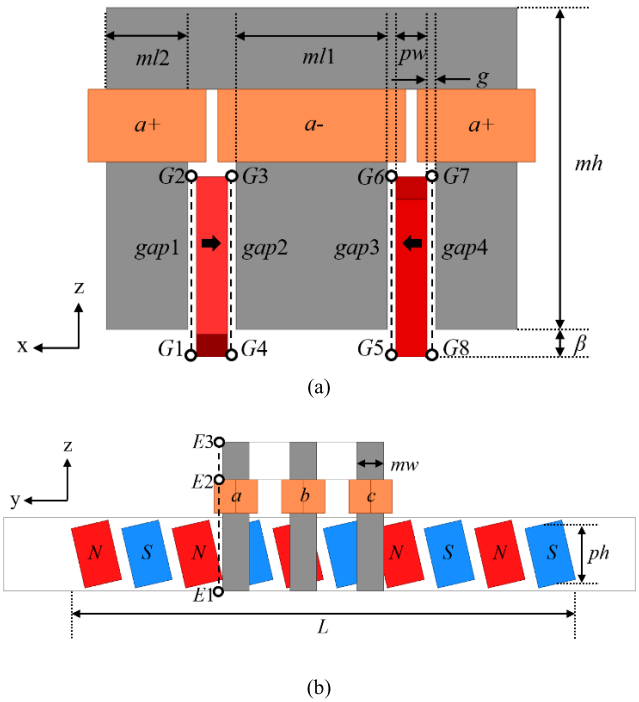


**FIGURE 4.** Design parameters. (a) Front view. (b) Side view.

**TABLE 1.** Design parameter of TLPMM.

| Parameter | Symbol |
|---|---|
| Center lag width (mm) | $ml1$ |
| Side lag width (mm) | $ml2$ |
| Mover height (mm) | $mh$ |
| Back-iron depth (mm) | $mw$ |
| Air-gap (mm) | $g$ |
| Overhang length (mm) | $\beta$ |
| Air-gap length (mm) | $L$ |
| PM depth (mm) | $pw$ |
| PM height (mm) | $ph$ |

### B. OPEN-CIRCUIT FIELD

On the other hand, in the case of $B_s$, the reference magnetic flux distribution is the open-circuit field generated by PM and requires FE analysis under no-load condition without excitation current. Fig. 3 shows the open-circuit field when the mover is in different positions from the initial position to 2 $\tau_p$. It can be seen that the air-gap flux distribution is distorted due to the change in reluctance while the mover moves by 2 $\tau_p$. Since the back-iron of the mover makes the air-gap magnetic flux distribution have a periodicity of 2 $\tau_p$, field information for 2 $\tau_p$ corresponding to one period is required. Therefore, sweeping of the basis function is performed as follows:

$$f_{s,h}(t, x, y, z) = f_{s,h}\left(t + \gamma\tau_p/n, x, y + \gamma\tau_p, z\right) \quad (7)$$

$$\gamma = 0, 1, 2, \ldots, \left(L_{stroke}/\tau_p - 1\right) \quad (8)$$

where $f_{s,h}$ is the basis function of the open-circuit field generated by the $h$th PM, $\gamma$ is the sweeping coefficient, and $L_{stroke}$ is the length of the stroke. $f_{s,h}$ is repeated every pole pitch.

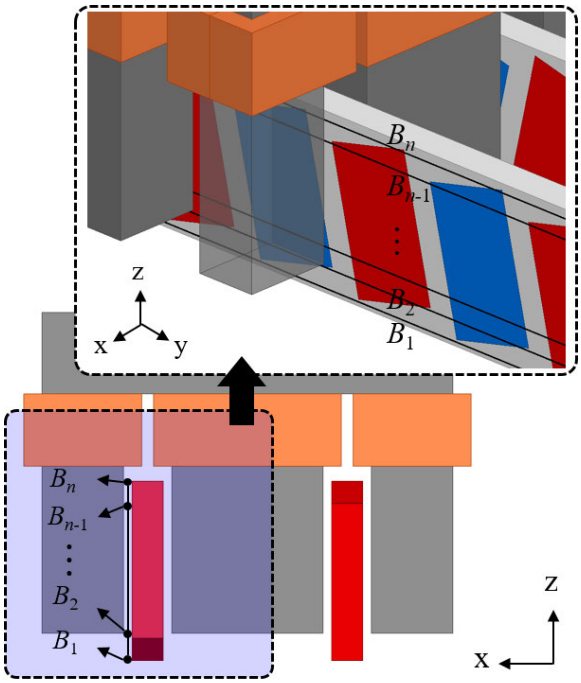


**FIGURE 5.** Virtual air-gap section.

### C. VIRTUAL AIR-GAP SECTION

Unlike the conventional LPMM and rotating machine with uniform magnetic flux density in the stacking direction, the TLPMM has different magnetic flux densities along the air-gap in $z$-direction. Fig. 4 shows the front and side views of the TLPMM. Table 1 presents the design parameter of the TLPMM. In Fig. 4 (a), the TLPMM has four effective air-gaps from $gap1$ to $gap4$. The four air-gaps are mirror-symmetry to each other about the central axis. However, the magnetic flux distribution in individual air-gaps is not uniform along the $z$-direction in Fig. 4. For example, over $gap1$, the magnetic flux density of $G1$ is different from that of $G2$ because it contains the magnetic flux leaking from the tip of the back-iron. In particular, because the TLPMM adopts the PM overhang to improve performance, the imbalance of magnetic flux density in this air-gap is extreme. Given that processing large amounts of data of all positions in the air-gap significantly increases the time cost, the proposed virtual air-gap section method can provide a reduction in computational burden by averaging the surrounding magnetic flux density. Fig. 5 shows the virtual air-gap sections in the $gap1$. The magnetic flux densities on the virtual air-gap section in the overhang region, the center and end regions of the PM are different. Therefore, the magnetic field of $gap1$ expressed by averaging the magnetic flux distribution of each virtual air-gap section can be obtained as follows:

$$B_{gap1}(x, y, z) = \frac{1}{n}\sum_{i=1}^{n} B_i(x, y, z_i) \quad (9)$$

where $B_i$ is the magnetic flux distribution on the $i$th virtual air-gap section, and $n$ is the number of virtual air-gap sections.

### D. FLUX LINKAGE

Most of the magnetic flux in the back-iron of the TLPMM is the flux entering the tooth. The magnetic flux entering the tooth can be considered as the magnetic flux passing through the middle air-gap. In the TLPMM, the back-irons of each phase are independent of each other because a non-magnetic material is inserted between them. Therefore, the flux linkage can be calculated as the flux density in the virtual tooth plane $\Delta z_a$ in Fig. 6. Since the magnetic flux entering the tooth is the $x$-directional component, the flux linkage is calculated as follows:

$$\lambda_a(t) = N_a \iint_{\Delta z_a} \left(B_{x,m}(x,y,z,t) + B_{x,s}(x,y,z,t)\right) dydz \tag{10}$$

where $\lambda_a$ and $N_a$ are the flux linkage and the number of turns in the $a$-phase winding, respectively. Using the voltage equation and flux linkage under no-load conditions, the back-EMF is calculated as follows:

$$\lambda_{no\,load}(t) = N_{abc} \iint_{\Delta z} B_{x,s}(x,y,z,t)\, dydz \tag{11}$$

$$e_{abc} = \frac{d\lambda_{no\,load}}{dt} \tag{12}$$

where $e_{abc}$ is the back-EMF of phase $abc$.

## IV. CHARACTERISTIC ANALYSIS OF TLPMM

The force calculation of the TLPMM can be obtained using the Maxwell stress tensor (MST) $\overleftrightarrow{T}$ as follows [21]:

$$F = \int_S \overleftrightarrow{T} \cdot \hat{n}\, dS \tag{13}$$

where $S$ is the surface area of the air-gap, $\hat{n}$ is the normal vector on the surface.

Each air-gap is shown along with design parameters in Fig. 4. Fig. 4 (a) shows a cross-sectional view when PM is the $N$-pole. The magnetization direction of the two PMs is toward the center leg. In this cross section, $B_{x,gap1}$ and $B_{x,gap2}$ are in the positive $x$-direction, and $B_{x,gap3}$ and $B_{x,gap4}$ are in the negative $x$-direction. If PM is the $S$-pole, $B_{x,gap1}$ and $B_{x,gap2}$ are in the negative $x$-direction, and $B_{x,gap3}$ and $B_{x,gap4}$ are in the positive $x$-direction. Therefore, if $B_{x,gap1}$ is positive, $B_{x,gap2}$ is always positive while $B_{x,gap3}$ and $B_{x,gap4}$ are negative. On the other hand, for $B_y$ in the $y$-direction, if $B_{y,gap1}$ is in the positive $y$-direction, then $B_{y,gap4}$ is in the positive $y$-direction while $B_{y,gap2}$ and $B_{y,gap3}$ are in the negative $y$-direction. Therefore, the thrust can be obtained as follows:

$$F_y = F_{y,gap1} + F_{y,gap2} + F_{y,gap3} + F_{y,gap4} \tag{14}$$

$$\begin{aligned} F_y = {} & \frac{1}{\mu_0} \int_L \int_{G1G2} B_{x,gap1} B_{y,gap1} dzdy \\ & - \frac{1}{\mu_0} \int_L \int_{G3G4} B_{x,gap2} B_{y,gap2} dzdy \\ & + \frac{1}{\mu_0} \int_L \int_{G5G6} B_{x,gap3} B_{y,gap3} dzdy \\ & - \frac{1}{\mu_0} \int_L \int_{G7G8} B_{x,gap4} B_{y,gap4} dzdy. \end{aligned} \tag{15}$$

where $L$ is the stack length in moving direction, and $\mu_0$ is the vacuum permeability. The attraction force is

$$F_x = F_{x,gap1} + F_{x,gap2} + F_{x,gap3} + F_{x,gap4} \tag{16}$$

$$\begin{aligned} F_x = {} & \frac{1}{2\mu_0} \int_L \int_{G1G2} \left(B_{x,gap1}^2 - B_{y,gap1}^2\right) dxdy \\ & - \frac{1}{2\mu_0} \int_L \int_{G3G4} \left(B_{x,gap2}^2 - B_{y,gap2}^2\right) dxdy \\ & + \frac{1}{2\mu_0} \int_L \int_{G5G6} \left(B_{x,gap3}^2 - B_{y,gap3}^2\right) dxdy \\ & - \frac{1}{2\mu_0} \int_L \int_{G7G8} \left(B_{x,gap4}^2 - B_{y,gap4}^2\right) dxdy \end{aligned} \tag{17}$$

If the absolute values of the magnetic flux density in each air-gap are similar, thrust and attraction force can be simplified as (15) and (16), respectively.

$$F_y \cong \frac{4}{\mu_0} \int_L \int_{G1G2} B_{x,gap1} B_{y,gap1} dzdy \tag{18}$$

$$F_x \cong 0. \tag{19}$$

Although the TLPMM has the advantage of having almost zero attraction force, it has still the detent force, which occurs due to structural characteristics of the TLPMM. This detent force is caused by slot effect and end effect [22], [23]. The detent force due to the slot effect is calculated in (19) when $B_x$ and $B_y$ consist only of open-circuit fields as follows:

$$F_{y,Detent} \cong \frac{4}{\mu_0} \int_L \int_{G1G2} B_{x,s,gap1} B_{y,s,gap1} dzdy \tag{20}$$

where $B_{x,s,gap1}$ and $B_{x,s,gap1}$ are the $x$- and $y$-direction components of the open-circuit field in $gap1$, respectively. On the other hand, the detent force due to the end effect can be calculated as

$$\begin{aligned} F_{eff} = {} & \frac{ml1}{2\mu_0} \int_{E1E2} \left(B_{y,eff}^2 - B_{x,eff}^2 - B_{z,eff}^2\right) dz \\ & + \frac{ml2}{\mu_0} \int_{E2E3} \left(B_{y,eff}^2 - B_{x,eff}^2 - B_{z,eff}^2\right) dz \end{aligned} \tag{21}$$

where $F_{eff}$ is the end force.

Therefore, the total detent force calculation in the TLPMM requires additional consideration of the end force as follows:

$$F_{total} = F_{y,Detent} + F_{eff,left} + F_{eff,right} \tag{22}$$

where $F_{total}$ is the total detent force in the TLPMM, and $F_{eff,left}$ and $F_{eff,right}$ are the end force obtained from the left and right end of the mover, respectively.

Fig. 7 shows $F_{eff}$ according to the position of the mover. The longitudinal end effect appears at both ends of the mover.

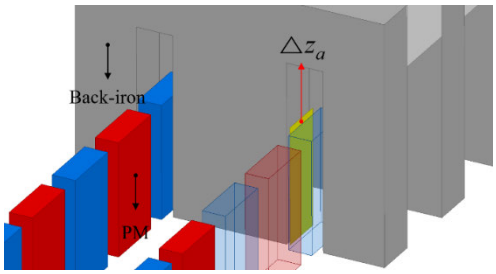


**FIGURE 6.** Virtual tooth plane.

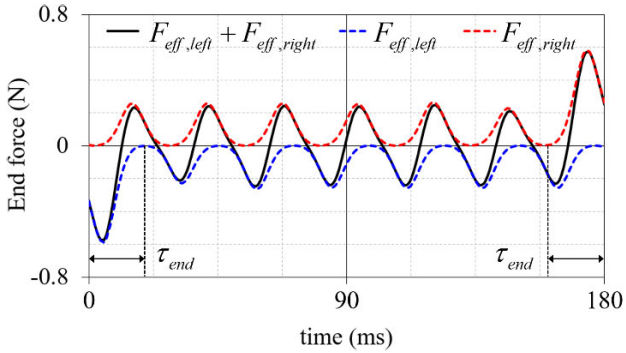


**FIGURE 7.** End force.

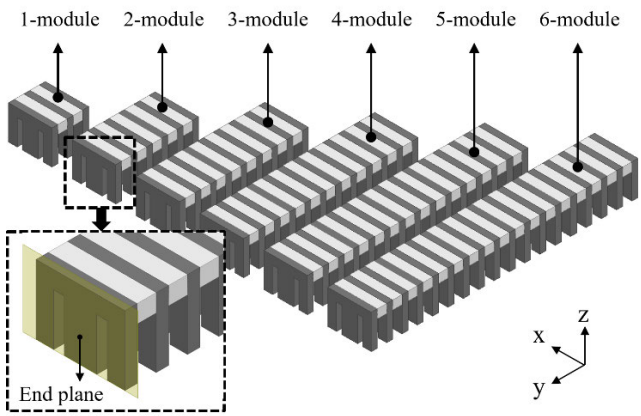


**FIGURE 8.** Mover modules.

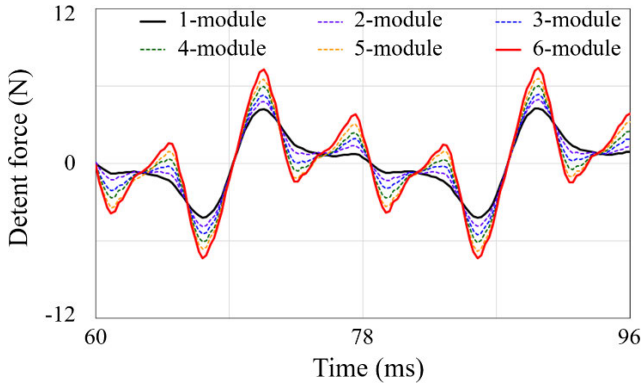


**FIGURE 9.** Detent force for mover modules.

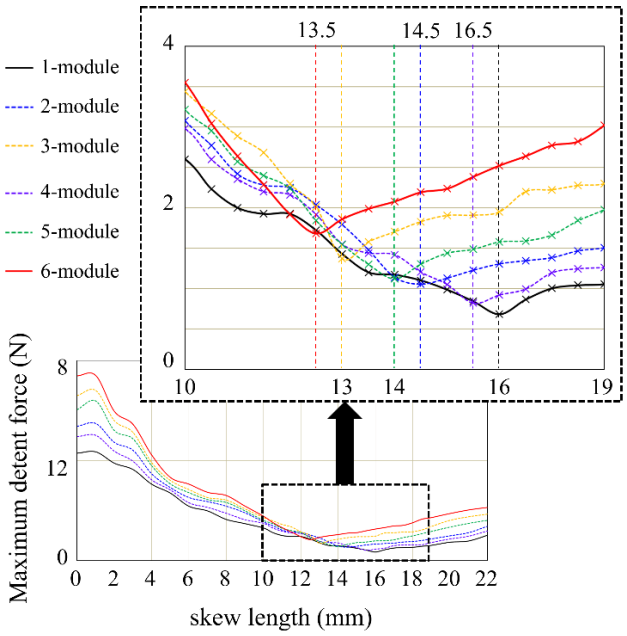


**FIGURE 10.** Maximum detent force for skew length in different modules.

It becomes significant when the mover begins to move away from the end of the stator and approaches the end of the stator. This effect is low when the mover is in the center of the stator. Therefore, the end effect can be larger in the LPMM and TLPMM with short strokes.

## V. PM SKEW AND OVERHANG OF TLPMM

Various studies have been developed to reduce the detent force. It is a well-known fact that PM skew is one of the effective methods. Unlike the PM skew of a general rotating machine, the PM skew of the LPMM can be represented by just rotating a rectangular PM. In the TLPMM, this PM rotation is used for the PM skew.

Since the stator and mover are composed of modules, the TLPMM has the advantage of being able to easily change the motor characteristics by changing the number of modules. As mentioned in section IV, LPMMs with the back-iron accompany the end force. As shown in Fig. 8, since the TLPMM has always two end plane regardless of the number of modules, the generated end force is maintained even if the number of modules of the mover is increased. On the other hand, the normal force related to the effective air-gap contributes more to the total detent force because the effective air-gap becomes longer as the number of modules is increased.

Therefore, the total detent force which is expressed as the sum of the end force and the normal force changes according to the number of modules. This results in a change in the skew length at which the detent force applied with the PM skew is minimized.

Fig. 8 shows back-irons with different number of modules in the mover of the TLPMM. The end plane of the back-iron is the same regardless of the number of modules, and the end force is calculated as (21). Fig. 9 shows the detent force of TLPMMs with different number of mover modules when PM was unskewed. The detent force was obtained using (22).

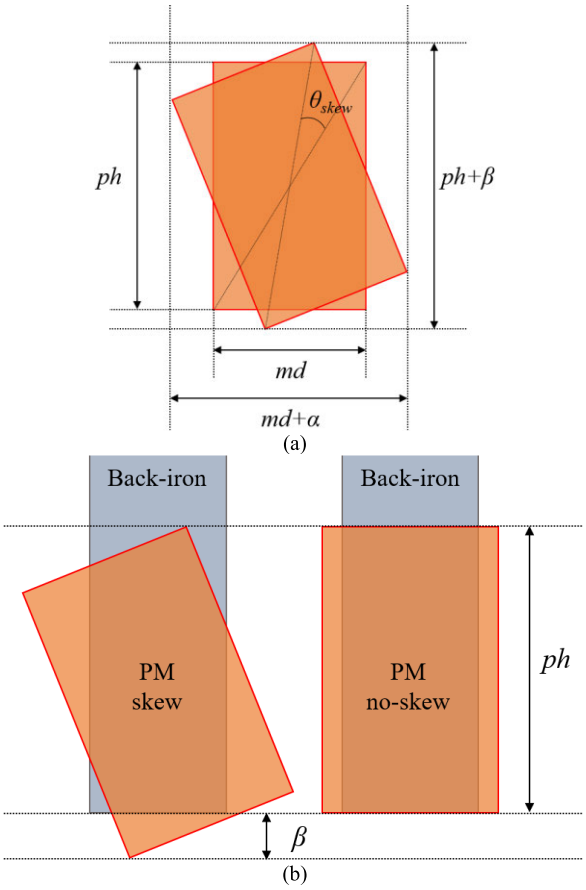


**FIGURE 11.** (a) PM skew. (b) PM overhang.

The end force is constant regardless of the number of modules, and the normal force was calculated using the air-gap magnetic flux distribution reconstructed by the basis function without additional FE analysis. The period of the end force is the pole pitch and the period of the normal force is the least common multiple of slot pitch and pole pitch [24].

Given that the number of poles and the number of slots in one module are 4 and 3, respectively, the end force and normal force in Fig. 9 should be repeated 2 and 6 times during one period for EMF, respectively. It is noted that as the module is increased, the influence of the end force involved in the overall detent force is decreased, and the period of the total detent force becomes shorter.

Fig. 10 shows the maximum value of detent force for skew lengths of TLPMMs with different number of mover modules. For 1-module TLPMMs, the optimal skew length is 16 mm, while for 6-module TLPMMs, the optimal skew length is 13.5 mm. This is because as the number of modules is increased, the period of the total detent force becomes shorter. As a result, it is required to determine an appropriate skew angle in order to select the number of modules of the TLPMM, and the field reconstruction method in Section III can be effectively used in terms of computational cost.

From rotating the PM by skew angles $\theta_{skew}$, both skew length $\alpha$ and overhang length $\beta$ are changed simultaneously

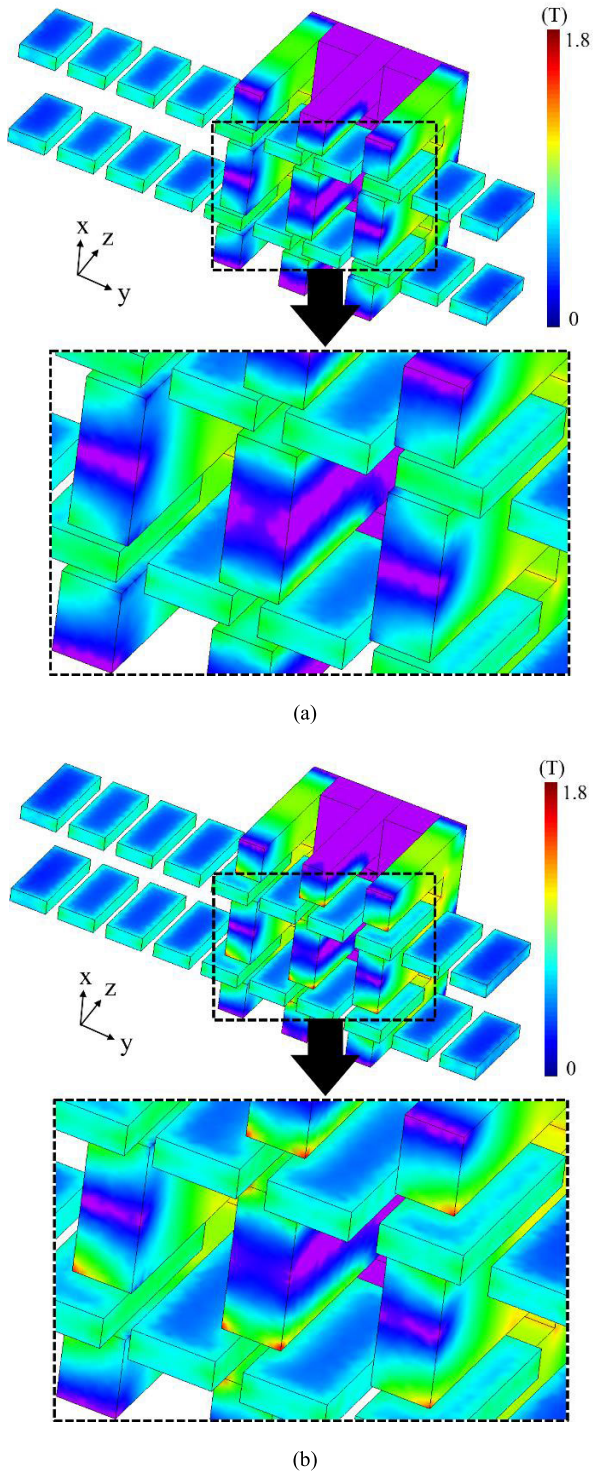


**FIGURE 12.** Magnetic flux density. (a) Non-overhang. (b) 5mm-overhang.

in Fig. 11 (a). Unlike the conventional LPMM, the overhang in the TLPMM is applied in only one direction as shown in Fig. 11 (b). This result makes it difficult to decide the optimal skew angle and overhang length.

The overhang structure compensates for the decrease in magnetic flux density due to leakage flux occurring at the end of the stack, thereby improving motor performance [17].

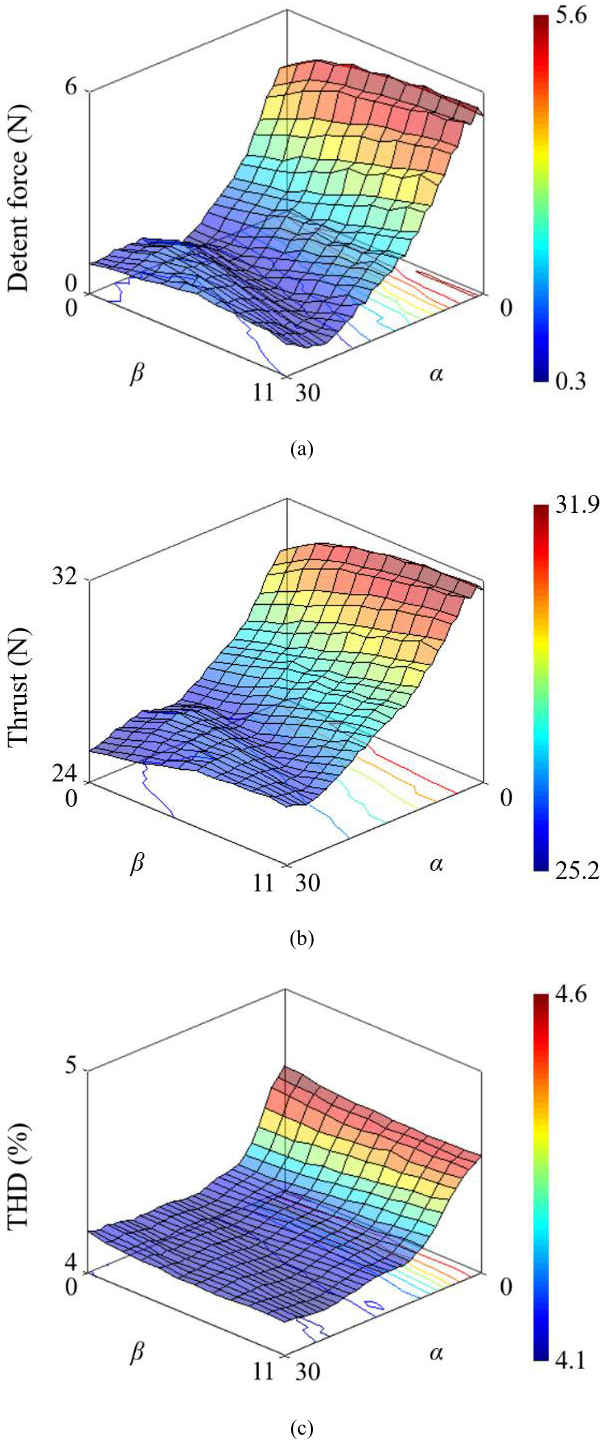


**FIGURE 13.** Comparative study results. (a) Detent force. (b) Thrust. (c) THD.

Fig. 12 (a) and (b) shows the magnetic flux density in the non-overhang model and the overhang model. The overhang structure provides additional magnetic flux and increases magnetic flux density at the end of the stack.

However, it should be taken into account that this overhang structure changes the optimal skew angle. This chapter presents the comparative studies for combinations between

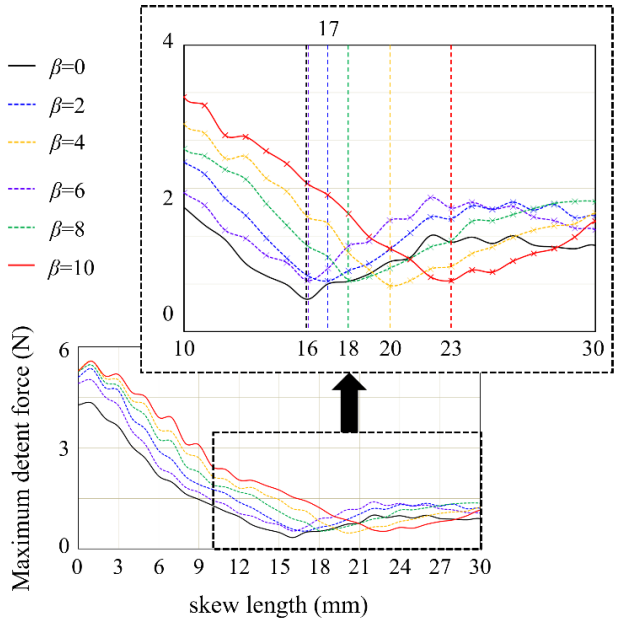


**FIGURE 14.** Maximum detent force for skew length in different overhang structures.

**TABLE 2.** Operating condition.

| | |
|---|---|
| Mover speed (m/s) | 1.0 |
| Rated current (A) | 10.0 |
| Rated voltage (V) | 95.0 |
| Frequency (Hz) | 55.5 |

overhang length and skew length through. Skew length $\alpha$ and overhang length $\beta$ are calculated as follows:

$$\alpha = (md - 1)\cos\theta_{skew} + ph\sin\theta_{skew} \tag{23}$$

$$\beta = (ph - 1)\cos\theta_{skew} + md\sin\theta_{skew} \tag{24}$$

where $md$ and $ph$ are the width and height of the PM, respectively as shown in Fig. 11. In the comparative analysis, $\theta_{skew}$ corresponding to each combination is calculated as

$$\theta_{skew} = \cos^{-1}\left(\frac{md}{\sqrt{md^2 + ph^2}}\right) - \cos^{-1}\left(\frac{md + \alpha}{\sqrt{md^2 + ph^2}}\right). \tag{25}$$

Fig. 13 shows the results of comparative analysis of the characteristics of the TLPMM. Table 2 shows the operating conditions of the comparative analysis. $\alpha$ and $\beta$ range from 0 to 30 and 0 to 11 respectively, and thrust and detent force represent the maximum values for $\alpha$ and $\beta$ combination.

The detent force in Fig. 13 (a) was calculated using (20). Overall, the detent force tends to decrease sharply as the skew length is increased. In Fig. 13 (a), the difference between the maximum value and the minimum value shows a reduction effect of 94.6%. However, it is noted that the optimal skew angle at which the detent force is minimized depends on the overhang length. Fig. 14 shows the maximum value of detent force for skew angles with different overhang lengths. The non-overhang TLPMM has an optimal skew length of 16 mm, while the TLPMM with an overhang length of 10 mm has

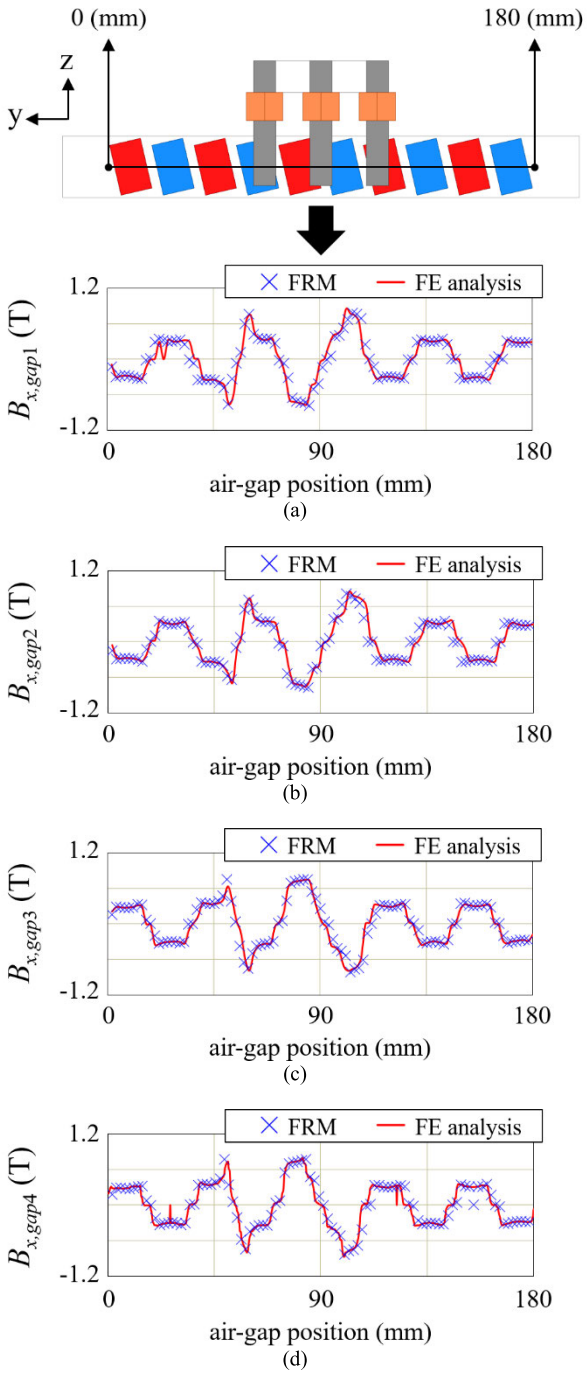


**FIGURE 15.** ***x*-component of air-gap magnetic flux distribution. (a) *gap*1. (b) *gap*2. (c) *gap*3. (d) *gap*4.**

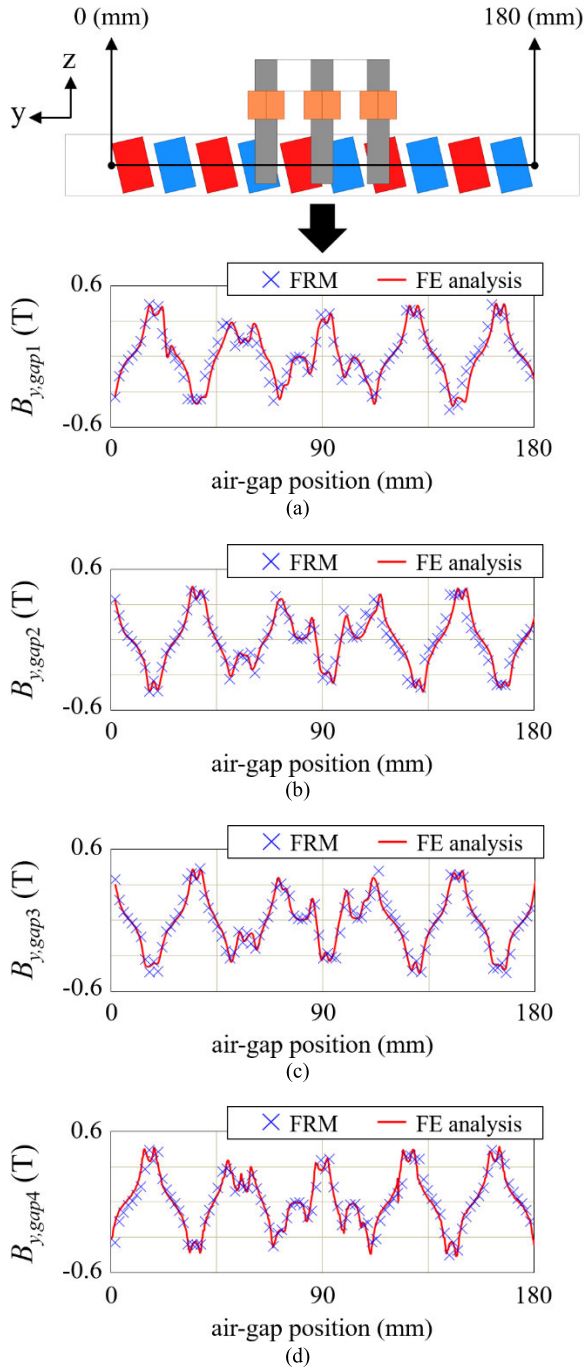


**FIGURE 16.** ***y*-component of air-gap magnetic flux distribution. (a) *gap*1. (b) *gap*2. (c) *gap*3. (d) *gap*4.**

an optimal skew length of 23 mm. The optimal skew length becomes longer as the overhang length is increased. This is because the overhang structure is longer than the length of the back-iron in $z$-direction, and the magnetic flux at the end of the stack changes its path, unlike the direct direction of the magnetic fluxes on the effective air-gap from the PM to the back-iron.

The overhang effect by the overhang structure improves the performance of the TLPMM, but not all magnetic fluxes in the overhang region contribute to the performance improvement. When the overhang length is increased, magnetic leakage flux is generated in the overhang region which is not directed to the back-iron of the mover. Therefore, the overhang length is not proportional to the motor performance, and the performance improvement due to the overhang structure is limited [25]. Fig. 13 (b) shows the maximum value of thrust according to the combination of $\alpha$ and $\beta$. The thrust in each combination was calculated using (14) and (15). It is

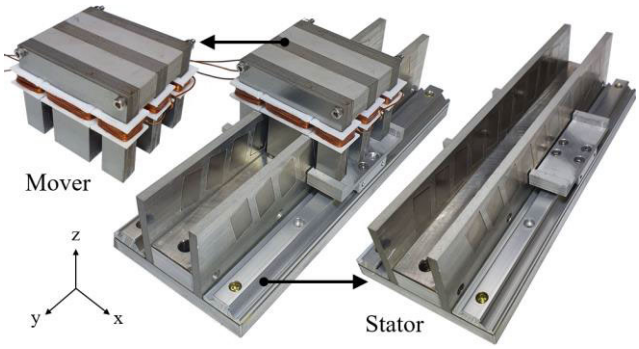


**FIGURE 17.** Prototype TLPMM.

**TABLE 3.** Basic specification of TLPMM.

| | |
|---|---|
| Center lag width, $ml1$ (mm) | 25 |
| Side lag width, $ml2$ (mm) | 13.5 |
| Mover height, $mh$ (mm) | 53.2 |
| Back-iron depth, $mw$ (mm) | 9.5 |
| Air-gap, $g$ (mm) | 1.45 |
| Air-gap length, $L$ (mm) | 180 |
| PM depth, $pw$ (mm) | 5.1 |
| PM height, $ph$ (mm) | 25 |
| Skew length, $\alpha$ (mm) | 6 |
| Overhang length, $\beta$ (mm) | 4 |
| Mover speed (m/s) | 1.0 |
| Rated current (A) | 10.0 |
| Rated voltage (V) | 95.0 |
| Frequency (Hz) | 55.5 |

noted that the degree of thrust improvement is decreased as the overhang length is increased. This is because either the magnetic flux density in the air-gap is saturated while the overhang length is increased, or the magnetic flux path between the PM and the back-iron becomes too long so that the magnetic flux does not go from the PM to the back-iron. Therefore, an accurate evaluation of its leakage flux is an important factor in determining the optimal overhang length.

In Fig. 13 (c), the THD of the back-EMF is calculated using (10)-(12). The THD is decreased as the skew length is increased, and the overhang length has no significant effect in the THD.

## VI. RESULT

Fig. 15 and 16 show the $x$- and $y$-components of the magnetic flux distribution, respectively. Table 3 shows the basic specifications of the TLPMM. The FE analysis was performed when the mover was positioned at the center of the stator, and the result of the FRM was reconstructed by the basis function.

In that FRM, the magnetic field sweep of the basis function was performed using the reference flux distribution at the initial position when the mover is positioned at the end of the stator. The $x$- and $y$-components of the magnetic flux density are important factors used in the calculation of thrust using (14) and (15) in Chapter IV. The difference between the FRM and FE analysis results is less than 5.3%.

Fig. 17 shows a prototype of the TLPMM. Fig. 18 shows the individual parts of the TLPMM. The test setup is shown in Fig. 19. The mover has one-module. It consists of three stacked back-irons and three-phase windings. Each winding

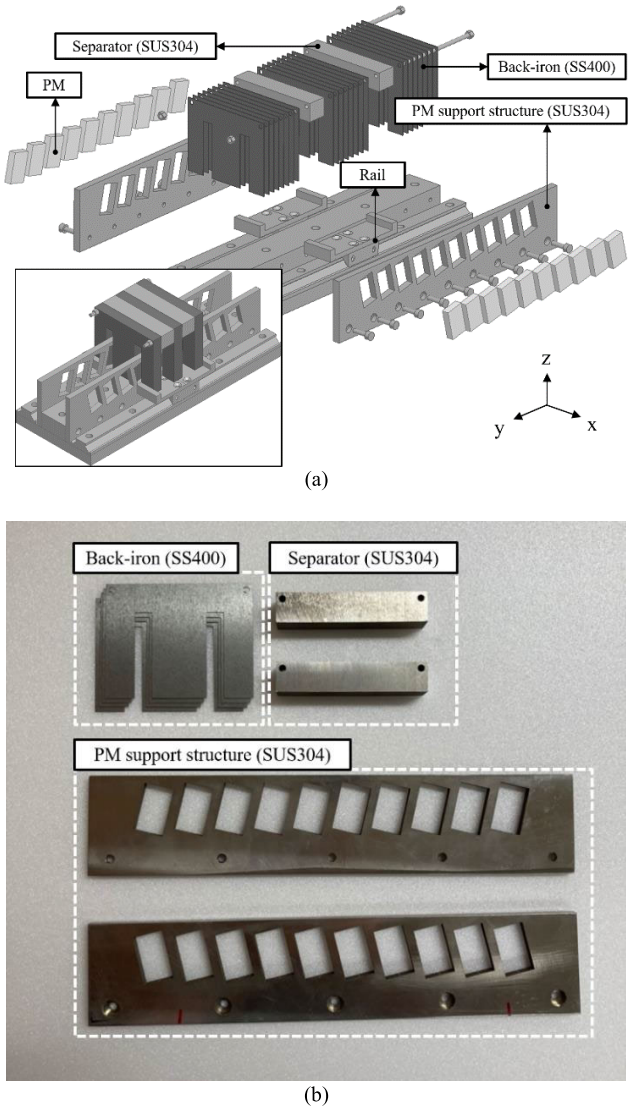


**FIGURE 18.** Components. (a) CAD. (b) Photograph.

is wound on the specially designed bobbin using 3D printer. The material of three back-irons is SS400. The back-irons corresponding to each phase are separated from each other by separators. Two holes were punched to assemble each component and positioned so as not to interfere with the magnetic flux path inside the back-iron. In the stator, the N40H was used for the PM and the skew length and overhang length were 6mm and 4mm respectively. The material of both the support structure and is non-magnetic SUS304.

In Fig. 20, the detent force calculated by the FRM is compared with the results of FE analysis and measurement. The mover was moved by a full stroke from one end of the stator to the other. In the FRM results, the detent force was calculated using (22), and the open-circuit field used for the calculation is the field reconstructed from (1)-(9).

As shown in Fig. 7, since the end force has a larger value at the beginning and end of the stroke, the detent force also shows the same pattern. Therefore, when the mover is

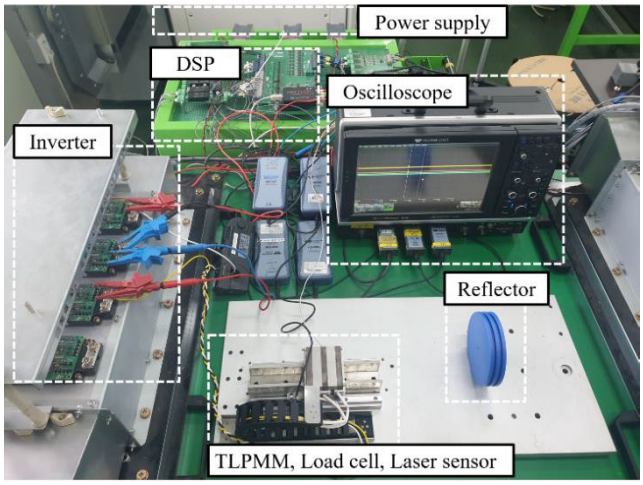


**FIGURE 19.** Test set.

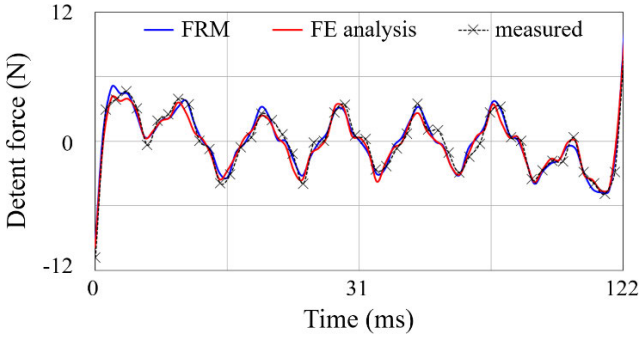


**FIGURE 20.** Detent force.

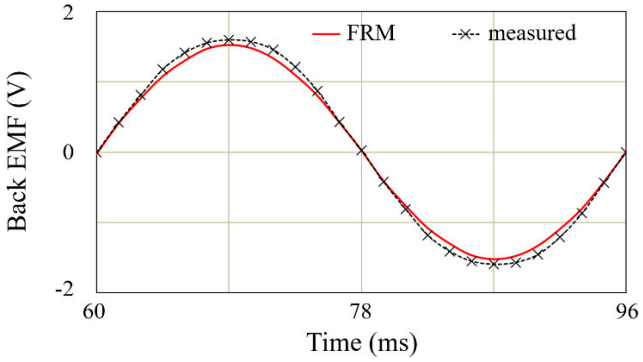


**FIGURE 21.** Back-EMF.

positioned at the center of the stator, it becomes periodic. The error between the results of the FRM and FE analysis is less than 1.5% and the error between the results of the FRM and the measurement result is less than 8.5%.

Fig. 21 shows the back-EMF. The back-EMF of the FRM was calculated in (12) using the magnetic flux density passing through the virtual tooth plane in the reconstructed open-circuit field. The results of the FRM had a difference of 5.6% compared to the measurement results.

Fig. 22 shows the thrust of the TLPMM. The thrust in each air-gap in Fig. 22 (a) is calculated from the reconstructed magnetic flux distribution in each air-gap using the virtual air-gap section method. The total thrust is

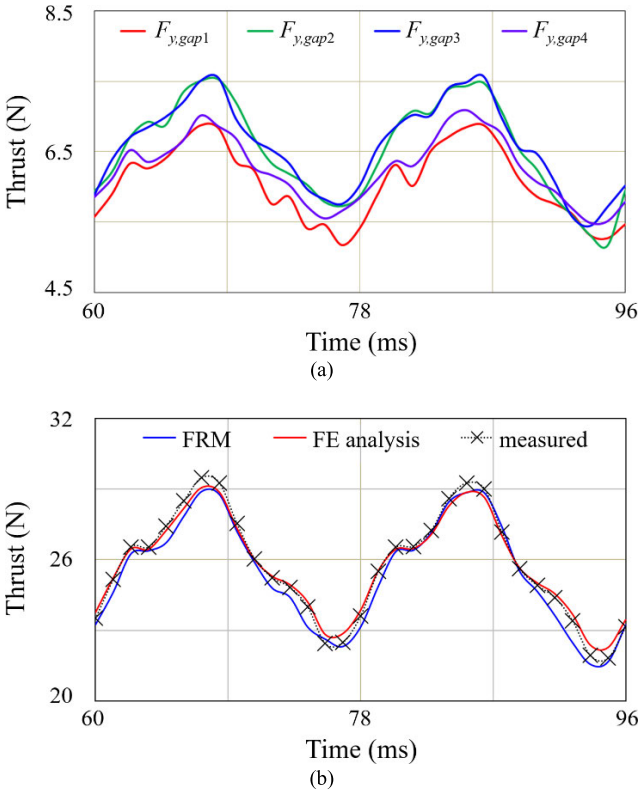


**FIGURE 22.** Thrust. (a) Individual air-gap. (b) Total thrust.

the sum of these individual air-gap thrusts as shown in Fig. 22 (b). Fig. 22 (b) shows the comparison results of the FRM, FE analysis, and measurement. Compared with the FE analysis results, the FRM obtained reasonable results with a difference of less than 2.1%. The difference from the measured value is 11.4%.

A force sensor is defined as a transducer that converts mechanical signals such as load and weight and tension and pressure into electrical output signals. This is commonly known as the load cell in Fig. 19, and is connected to a digital indicator that provides equivalent thrust. In the test setup, the load cell detects the thrust at a specific mover position. The laser sensor is used to set the specific position of the TLPMM. First, set the reference position of the mover to the back-EMF zero-crossing point. The applied current value changes according to the moving distance of the mover from the reference position. During the stroke of the TLPMM, the specific current value corresponding to the position of the mover is applied repeatedly.

Under the same simulation conditions (CPU Intel core i7-11700K, GPU RTX 3060 Ti, RAM 32GB, Elements 62702), the FE analysis required 5h 32m to analyze the full stroke as shown in Fig. 18, while the FRM took 1h 28m, including the FE analysis to obtain a reference magnetic flux distribution. The FRM provided a 73.5% reduction in computation time. Furthermore, this can provide a significant time-cost reduction when analyzing TLPMMs with a large number of modules or in the optimization process such as finding the optimal skew and overhang length.

## VII. CONCLUSION

This paper introduced the TLPMM with the novel structure. Since the magnet skew and overhang structures require 3D analysis for characterization, the proposed magnetic field analysis method significantly reduces the computational burden. For each of the four air-gaps, the magnetic flux densities in the z-direction were non-uniform, and the value of the magnetic flux density in the effective air-gap was calculated using the virtual air-gap section method.

The thrust and detent force and flux linkage were calculated using the reconstructed magnetic field. The end force was analyzed due to end effects at both ends of the back-iron. Especially, this affected the optimal skew angle as it contributes to the overall detent force.

Finally, the optimal skew angle of the TLPMM was investigated, depending on the number of modules and the length of the overhang. Characteristics of the TLPMM with respect to the overhang length and the skew length were provided through the comparative analysis.

The proposed method provided good accuracy with a reduction in computation time. This method can be valuable tool for the TLPMMs and LPMMs with other complex structures in design and analysis.

## REFERENCES

[1] A. Boduroglu, Y. Demir, B. Cumhur, and M. Aydin, "A novel track structure of double-sided linear PM synchronous motor for low cost and high force density applications," *IEEE Trans. Magn.*, vol. 57, no. 2, pp. 1–5, Feb. 2021.

[2] B. L. J. Gysen, K. J. Meessen, J. J. H. Paulides, and E. A. Lomonova, "Semi-analytical calculation of the armature reaction in slotted tubular permanent magnet actuators," *IEEE Trans. Magn.*, vol. 44, no. 11, pp. 3213–3216, Nov. 2008.

[3] S. W. Youn, J. J. Lee, H. S. Yoon, and C. S. Koh, "A new cogging-free permanent-magnet linear motor," *IEEE Trans. Magn.*, vol. 44, no. 7, pp. 1785–1790, Jul. 2008.

[4] S. G. Min, "Integrated design method of linear PM machines considering system specifications," *IEEE Trans. Transport. Electrific.*, vol. 7, no. 2, pp. 804–814, Jun. 2021.

[5] I. I. Abdalla, T. Ibrahim, and N. M. Nor, "Analysis of tubular linear motors for different shapes of magnets," *IEEE Access*, vol. 6, pp. 10297–10310, 2018.

[6] K. H. Kim and D. K. Woo, "Linear tubular permanent magnet motor for an electromagnetic active suspension system," *IET Electr. Power Appl.*, pp. 1–18, Sep. 2021.

[7] K.-H. Kim and D.-K. Woo, "Field reconstruction method for linear tubular permanent magnet motor," *IEEE Access*, vol. 8, pp. 169516–169524, 2020.

[8] H.-J. Park, H.-K. Jung, S.-Y. Jung, Y.-H. Chae, and D.-K. Woo, "Field reconstruction method in axial flux permanent magnet motor with overhang structure," *IEEE Trans. Magn.*, vol. 53, no. 6, pp. 1–4, Jun. 2017.

[9] E. Ajily, K. Abbaszadeh, and M. Ardebili, "Three-dimensional field reconstruction method for modeling axial flux permanent magnet machines," *IEEE Trans. Energy Convers.*, vol. 30, no. 1, pp. 199–207, Mar. 2015.

[10] M. Inoue and K. Sato, "An approach to a suitable stator length for minimizing the detent force of permanent magnet linear synchronous motors," *IEEE Trans. Magn.*, vol. 36, no. 4, pp. 1890–1893, Jul. 2000.

[11] K.-C. Lim, J.-K. Woo, G.-H. Kang, J.-P. Hong, and G.-T. Kim, "Detent force minimization techniques in permanent magnet linear synchronous motors," *IEEE Trans. Magn.*, vol. 38, no. 2, pp. 1157–1160, Mar. 2002.

[12] A. Boduroglu, Y. Demir, R. Lyra, and M. Aydin, "Influence of auxiliary teeth on performance of a permanent magnet linear motor," in *Proc. 13rd Int. Conf. Electr. Mach. (ICEM)*, Sep. 2018, pp. 779–784.

[13] A. Boduroglu, M. Gulec, Y. Demir, E. Yolacan, and M. Aydin, "A new asymmetric planar V-shaped magnet arrangement for a linear PM synchronous motor," *IEEE Trans. Magn.*, vol. 55, no. 7, pp. 1–5, Jul. 2019.

[14] M. Aydin and M. Gulec, "Reduction of cogging torque in double-rotor axial-flux permanent-magnet disk motors: A review of cost-effective magnet-skewing techniques with experimental verification," *IEEE Trans. Ind. Electron.*, vol. 61, no. 9, pp. 5025–5034, Sep. 2014.

[15] D.-K. Woo and B. H. Jeong, "Irreversible demagnetization of permanent magnet in a surface-mounted permanent magnet motor with overhang structure," *IEEE Trans. Magn.*, vol. 52, no. 4, pp. 1–6, Apr. 2016.

[16] Y.-Y. Ko, J.-Y. Song, M.-K. Seo, W. Han, Y.-J. Kim, and S.-Y. Jung, "Analytical method for overhang effect of surface-mounted permanent-magnet motor using conformal mapping," *IEEE Trans. Magn.*, vol. 54, no. 11, pp. 1–5, Nov. 2018.

[17] K.-H. Kim, B. H. Jeong, and D.-K. Woo, "Optimal overhang structure considering overhang effects in the axial flux permanent magnet motor," *Int. J. Appl. Electromagn. Mech.*, vol. 58, no. 2, pp. 227–237, Aug. 2018.

[18] H.-K. Yeo, D.-K. Lim, D.-K. Woo, J.-S. Ro, and H.-K. Jung, "Magnetic equivalent circuit model considering overhang structure of a surface-mounted permanent-magnet motor," *IEEE Trans. Magn.*, vol. 51, no. 3, pp. 1–4, Mar. 2015.

[19] M. M. Kiani, W. Wang, and W.-J. Lee, "Elimination of system-induced torque pulsations in doubly-fed induction generators via field reconstruction method," *IEEE Trans. Energy Convers.*, vol. 30, no. 3, pp. 1228–1236, Sep. 2015.

[20] E. Ajily, M. Ardebili, and K. Abbaszadeh, "Magnet defect and rotor eccentricity modeling in axial-flux permanent-magnet machines via 3-D field reconstruction method," *IEEE Trans. Energy Convers.*, vol. 31, no. 2, pp. 486–495, Jun. 2016.

[21] A. Souissi, I. Abdennadher, A. Masmoudi, F. Marignetti, and R. Di Stefano, "Feature investigation of a T-LPMSM following the selection of its slot-pole combination," *IEEE Trans. Ind. Appl.*, vol. 53, no. 2, pp. 1009–1017, Mar. 2017.

[22] S. G. Min and B. Sarlioglu, "Analytical calculation of back EMF waveform for linear PM motors in slotted and slotless structures," *IEEE Trans. Magn.*, vol. 53, no. 12, pp. 1–10, Dec. 2017.

[23] S. G. Min and B. Sarlioglu, "Analytical prediction and multiconstrained nonlinear optimization of slotted linear PM motors taking into account two-dimensional end effects," *IEEE Trans. Ind. Electron.*, vol. 67, no. 4, pp. 2965–2976, Apr. 2020.

[24] G. Bramerdorfer, E. Marth, and G. Goldbeck, "Cogging torque sensitivity considering imperfect magnet positioning for permanent magnet machines of different slot and pole count," *CES Trans. Electr. Mach. Syst.*, vol. 4, no. 3, pp. 243–251, Sep. 2020.

[25] D.-K. Woo, D.-K. Lim, H.-K. Yeo, J.-S. Ro, and H.-K. Jung, "A 2-D finite-element analysis for a permanent magnet synchronous motor taking an overhang effect into consideration," *IEEE Trans. Magn.*, vol. 49, no. 8, pp. 4894–4899, Aug. 2013.